



Cavitation bubble structures below a soft boundary in an ultrasonic field

Fan Li, Chenyang Huang, Xianmei Zhang, Chenghui Wang^{*}, Jing Hu, Shi Chen, Hua Tian, Zhuangzhi Shen, Jianzhong Guo, Shuyu Lin

Institute of Shaanxi Key Laboratory of Ultrasonics, Shaanxi Normal University, Xi'an 710119, China

ARTICLE INFO

Keywords:

Layer bubble clusters
Soft boundary
Bjerknes force
Bifurcation diagram

ABSTRACT

We studied the layer structure of bubbles just below water/air and water/EPE (Expandable polyethylene) interfaces using high-speed photography. The layer structure was generated by floating spherical clusters, the source bubbles of which were identified to come from the attachment of bubble nuclei at the interface, the floating of bubbles in the bulk liquid, or bubbles generated on the surface of the ultrasonic transducer. The boundary shape affected the layer structure, which assumed a similar profile below the water/EPE interface. We developed a simplified model composed of a bubble column and bubble chain to describe interface impacts and the interaction of bubbles in a typical branching structure. We found that the resonant frequency of the bubbles is smaller than that of an isolated single bubble. Moreover, the primary acoustic field plays an important role in the generation of the structure. A higher acoustic frequency and pressure were found to shorten the distance between the structure and the interface. A hat-like layer structure of bubbles was more likely to exist in the low-frequency (28 and 40 kHz) intense inertial cavitation field, in which bubbles oscillate violently. By contrast, structures composed of discrete spherical clusters were more likely to form in the relatively weak cavitation field at 80 kHz, in which stable and inertial cavitation coexisted. The theoretical predictions were in good agreement with the experimental observations.

1. Introduction

Acoustic cavitation, the expansion and collapse of newly formed bubbles, which leads to localized hot spots and high pressure [1] is the dynamic source of sonochemistry. This is widely applied in ultrasonic cleaning [2], ultrasonic atomization [3], water treatment [4], and other fields. The dynamic behavior of cavitation bubbles plays a critical role in the utilization of cavitation energy. Therefore, fully understanding the dependence of bubbles on the acoustic field is of great significance.

Bubbles are driven to translate and pulsate radially by ultrasound, and they can aggregate to form different structures, such as cone clusters, streamers, and layer structures (e.g. jellyfish and starfish structures). Experimental observations have demonstrated that the morphology of the cavitation structure depends on the acoustic field and boundary conditions [5]. Just below the free surface of the cavitating water, a layer structure of bubbles can be observed in ultrasonic cleaners, which is composed of spherical clusters and multilevel branching chains [6]. Two theoretical approaches have been proposed to investigate the formation mechanism of the layer structure [7–13]. This first is the theory of the effective medium, which was introduced to

explore acoustic propagation in a bubbly liquid, where the bubble concentration of the branching structure can be predicted using a one-dimensional model [7,8]. In the second approach, bubbles are treated as particles, the trajectories of which are simulated by calculating the Bjerknes force and the drag force on the bubbles [9–13]. The results of this approach have shown good agreement with experimental observations. Li [14] developed a theoretical model of the bubble chain to explain bubble transportation in an acoustic Lichtenberg figure by considering the effect of a bubble equivalent radius and acoustic field on the stability of the structure.

The bubble behavior and the morphology of the bubble structure are significantly influenced by the properties of the boundary (in particular, whether it is soft or hard) [15–17]. When bubbles oscillate near hard (soft) boundaries, their resonant frequency might be lower (higher) than the Minnaert frequency of bubbles in an unbounded liquid [16,17]. The acoustic resonant response of bubbles is important for predicting nonlinear bubble–bubble interactions, which are closely related to the stability of the bubble structure [14]. When the acoustic pressure is low, bubbles are repelled from each other if the driving frequency lies between the respective resonant frequencies of the bubbles; otherwise,

^{*} Corresponding author.

E-mail address: wangld001@snnu.edu.cn (C. Wang).

<https://doi.org/10.1016/j.ultsonch.2023.106500>

Received 27 February 2023; Received in revised form 2 June 2023; Accepted 19 June 2023

Available online 23 June 2023

1350-4177/© 2023 The Author(s). Published by Elsevier B.V. This is an open access article under the CC BY-NC-ND license (<http://creativecommons.org/licenses/by-nc-nd/4.0/>).

they experience attraction [18]. However, the effect of soft boundaries on bubble behavior has not been considered in detail in previous studies, despite layer clusters being clearly observed near soft boundaries [5,6]. An appropriate theory needs to be established to explain these cavitation phenomena, which may help to understand the mechanisms that underpin various applications of cavitation, such as ultrasonic therapy or ultrasonic extraction of herbs [19].

In this paper, we experimentally investigated the effect of acoustic intensity and frequency on the layer structures in tap water just below water/air and water/EPE (Expand aple poly ephylene) interfaces. We also developed a simplified theoretical model to describe bubble–bubble interactions and explain the hovering phenomenon of the layer structure of bubbles. The model explained the observed phenomena very well.

2. Experimental observations

A transparent tank ($100 \times 100 \times 300 \text{ mm}^3$) with a water depth of 250 mm was placed in an ultrasonic cleaner ($320 \times 300 \times 200 \text{ mm}^3$) with frequencies of 28, 40, and 80 kHz. The maximum electric power of the baths was 360 W. The evolution of bubble clusters below the free surface of the tap water with many gas nuclei was observed in this tank using a high-speed camera (i-SPEED 726, iX Cameras Ltd. UK) at 20,000 fps. Similarly, videos of the bubble structure below a piece of EPE ($94 \times 94 \times 25 \text{ mm}^3$) partly immersed in the water were captured by the camera, with the bubble structure backlit by the illumination system (DannyU high power LED light), as shown in Fig. 1.

Ultrasound with a frequency of 28 kHz was radiated from transducers mounted at the bottom of the ultrasonic cleaner and reflected on the free water surface, forming a standing wave in the water. When the machine was operated at 360 W, cavitation was excited and many bubbles were observed in the water. Bubbles aggregated into multi-

shaped clusters, and many spherical bubble clusters appeared in the bulk liquid (Fig. 2(b)). Spherical clusters floated to a height of about 4 mm below the water surface (Fig. 2(c)), and spread out by attracting surrounding bubble nuclei, which then formed a thin layer structure (Fig. 2(e)). The horizontal morphology of the layer structure is shown in Fig. 3(a). The bubbles moved along the branches towards the inner region of the structure, where they merged into large bubbles or spherical clusters. These newly generated large bubbles (clusters) rose up and collapsed below the free surface, which led to an upward water bulge. Because of the coupled interaction, a hat-like concave shape appeared in the middle of layer structure 1 in Fig. 2(f). Notably, more than one structure may appear at the same time. Fig. 2(f) presents the appearance of two separated small structures marked by '2' and '3' on either side of layer structure 1. These structures may have been generated by the inhomogeneous horizontal distribution of acoustic pressure, which may have led to the existence of more than one aggregation center [6]. In general, the layer structure observed by the naked eye was accompanied by several separated structures and had the appearance of a millipede. This was similar below EPE, as shown in Fig. 4.

On the basis of the videos, we identified two mechanisms by which the layer structure of bubbles formed: (1) a rising spherical cluster suddenly expands at a certain height and then hovers at that height; and (2) the attached bubbles are ejected from the interface and rapidly translate in the bulk liquid, attracting bubble nuclei to form spherical clusters, which aggregate into a whole structure and evolve into a layer structure, as shown in Fig. 5. These phenomena were observed at both the air/water or EPE/water interface. The upper row displays a bubble with a radius $\sim 34 \mu\text{m}$ moving away from the free surface (marked by the red circle in Fig. 5(a1)). The bubble first moved downward (Fig. 5(a2–a4)), and then rose to a height of about 4 mm below the interface (Fig. 5(a4–a6)). The red line represents the trajectory. Because the

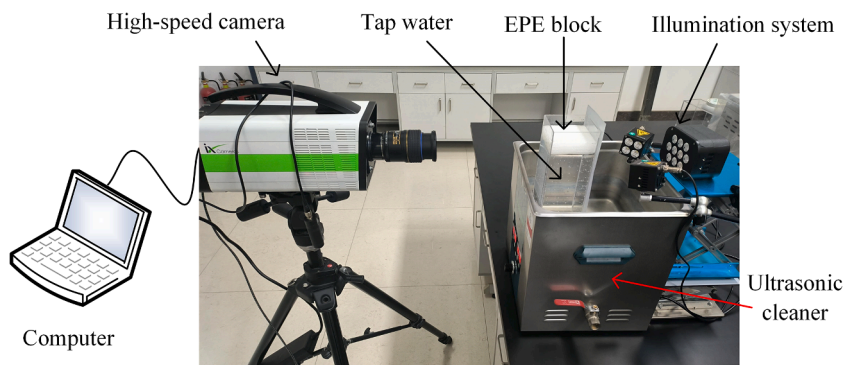


Fig. 1. Experimental setup.

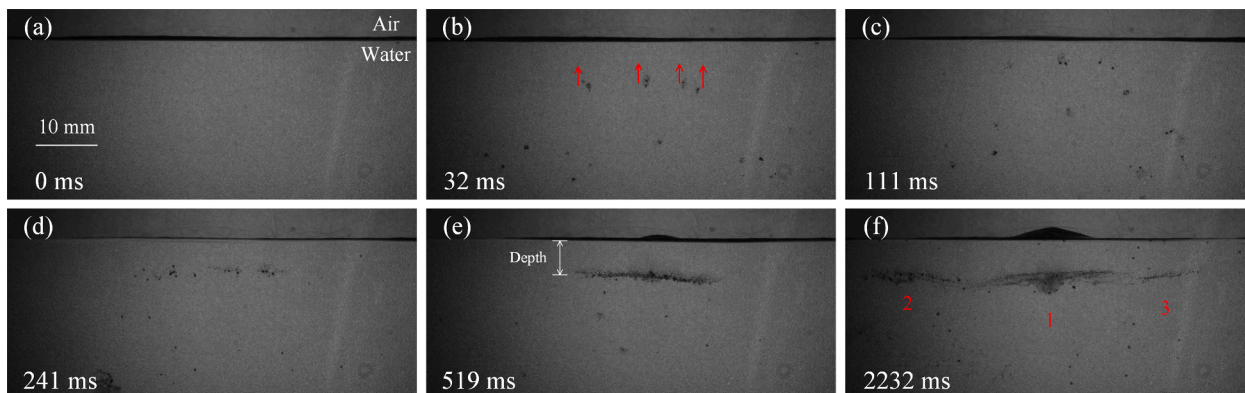


Fig. 2. Formation of a layer structure under the free water surface (Supplementary video 1; framerate of 1000 fps). The frequency was 28 kHz and the electric power was 360 W. The red arrows represent the direction of motion of the spherical bubble clusters.

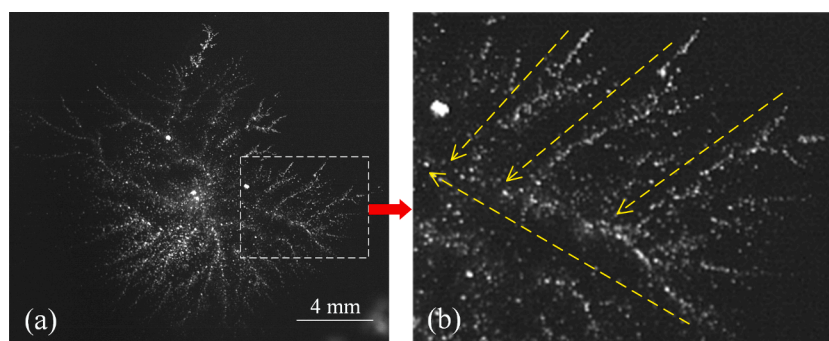


Fig. 3. Horizontal morphology of the layer bubble cluster (scattered light). The acoustic frequency was 28 kHz and the electric power was 360 W. Panel (b) is an enlarged picture of region of panel (a), which is marked by the dashed box. The yellow dashed arrows represent the path of motion of the bubbles.

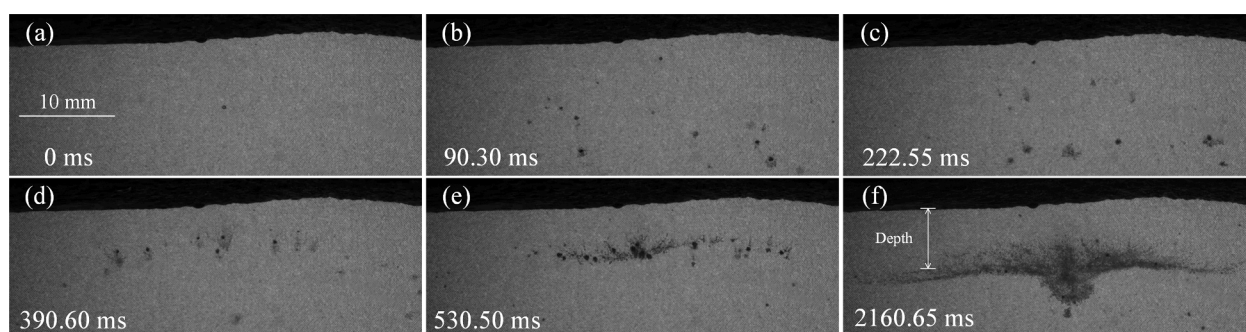


Fig. 4. Formation of a bubble cluster under the EPE/water interface (Supplementary video 2). The frequency was 28 kHz and electric power was 360 W.

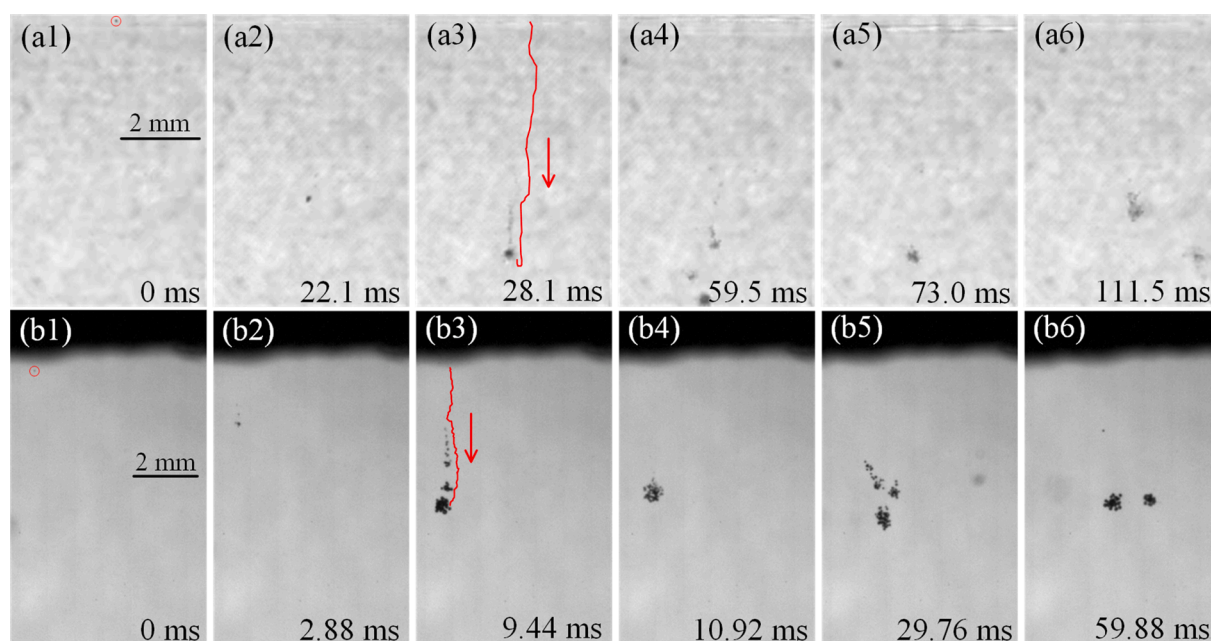


Fig. 5. Formation of spherical bubble clusters (backlit): (a) under a free surface (Supplementary video 3) and (b) under an EPE/water interface (Supplementary video 4 with a framerate of 25,000 fps). The frequency was 28 kHz and electric power was 360 W. The black object on the top side of the images is EPE. The red lines and arrows represent the trajectory of small bubbles or clusters.

surrounding bubble nuclei were attracted to this moving bubble, tadpole-like bubble aggregation could be observed (Fig. 5(a3)) [14]. Gradually, bubble clusters formed. Similar phenomena appeared in the water covered by the EPE (bottom row in Fig. 5). However, tadpole-like bubble aggregation occurred more quickly. We predicted that there were more bubble nuclei attached at the EPE surface [20]. Therefore,

the aggregating behavior could be enhanced by the high density of the bubble nuclei. Moreover, more complex interactions were found between the new clusters, which affected their evolution and structure shape. Interestingly, the tailing bubbles of the tadpole-like structure could be quickly absorbed into the head cluster, thereby expanding the head cluster (Fig. 5(b3, b4)). This large cluster acted as an

attractor of bubbles, leading to the formation of group of bubble clusters (Fig. 5(b5, b6)).

After a period of time, many bubbles accumulated below the EPE/water interface and formed a layer structure (Fig. 6(a)). The shape of the structure was similar to that of the boundary (marked by the two nearly parallel curves in Fig. 6(a)). The surrounding gas nuclei accumulated into this structure, which resulted in an increase of the bubble concentration followed by bubble coalescence. The rise of many coalescing bubbles toward the interface led to a relatively stable bubble concentration in this structure. Because the acoustic frequency influences the cavitation threshold, fewer cavitation nuclei might be excited as the frequency increases. Comparing Fig. 4(d) and Fig. 6(b), the accumulating bubble distribution at 80 kHz was similar to that during the initial stage of cavitation at 28 kHz. Because of the limited electrical power of the ultrasonic bath at 80 kHz (maximum power: 360 W), the cavitation intensity was insufficiently strong to obtain a whole structure similar to that formed at 28 kHz (Fig. 4(f)). The aggregation morphology and evolution of bubbles below the air/water and EPE/water interfaces were markedly different from those below a hard boundary, where the bubbles clusters rushed to and strongly impacted the surface, as shown in Appendix A. Therefore, the layer structure of bubbles only appears below a soft interface in the cavitation field.

Comparison of Fig. 4(f) and Fig. 6 reveals that the depth of these structures (marked in Fig. 2(e) and Fig. 4(f)) is influenced by the frequency. Because forming a layer structure below the free water surface at 80 kHz was difficult, the depth under the EPE/water interface was measured at 28, 40, and 80 kHz, as shown in Fig. 7(a). The depth decreased with increasing acoustic frequency. Higher frequency, shorter wavelength, which might be the cause of this phenomenon. Moreover, an increase in acoustic pressure led to a decrease in the depth of the

cavitation structure at 28 kHz, as shown in Fig. 7(b). Therefore, we predicted that the acoustic pressure and frequency should have a synergistic effect on the evolution of the layer structure. The weighted average depth of the layer structure below the EPE/water interface (5.63 mm) was similar to that below the air/water interface (5.90 mm) at 28 kHz and 360 W; however, the lengths of the bars, which are representative of the vertical floating range of the structure, were not equal. The vertical fluctuation might be related to the interaction between the structure and the interface, which affects the distribution of the radiation field. Moreover, local deformation of the air/water interface may lead to a repulsive effect within the structure, causing a hat-like shape to form. We can reasonably predict that high-intensity, high-frequency ultrasound generates a large number of cavitation bubbles near a soft interface to enhance the effects of cavitation [21].

The structure of the accumulated bubbles just below the air/water and EPE/water interfaces in the ultrasonic cavitation field was either a layer or spherical. Many structures may coexist at a given depth from the interface, which may coalesce or remain separate. The frequency and the acoustic intensity are the main parameters that affect the evolution of these clusters. However, the properties of the medium and the boundary characteristics also have important roles in the formation of these bubble structures. To understand the mechanisms by which these structures float stably below the interface in the cavitation field, we developed a simplified theoretical model, which is described in the next section.

3. Theoretical analysis

In the top-view pictures, a typical branching structure can be observed, in which each branch is the travel path of the bubbles. The

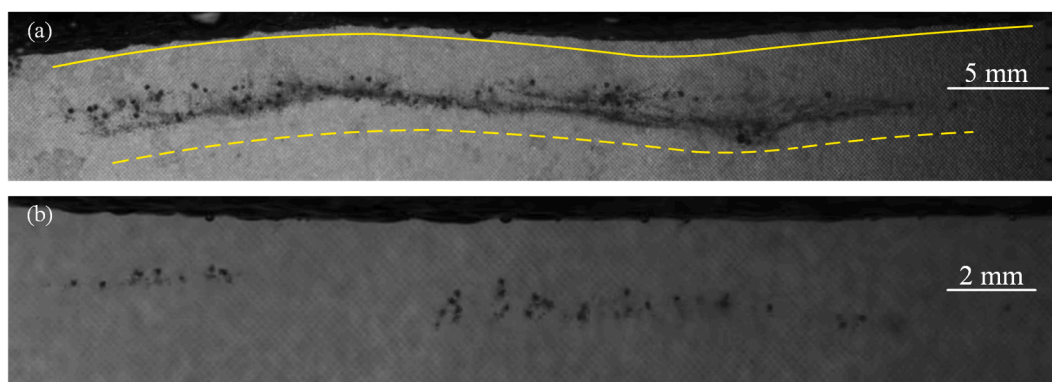


Fig. 6. Bubble clusters below the EPE/water interface at (a) 40 kHz (Supplementary video 5) and (b) 80 kHz (Supplementary video 6). The input electric power was 360 W. The solid and dashed yellow curves represent the profile of the interface and layer structures. The black object on the top side of the images is EPE.

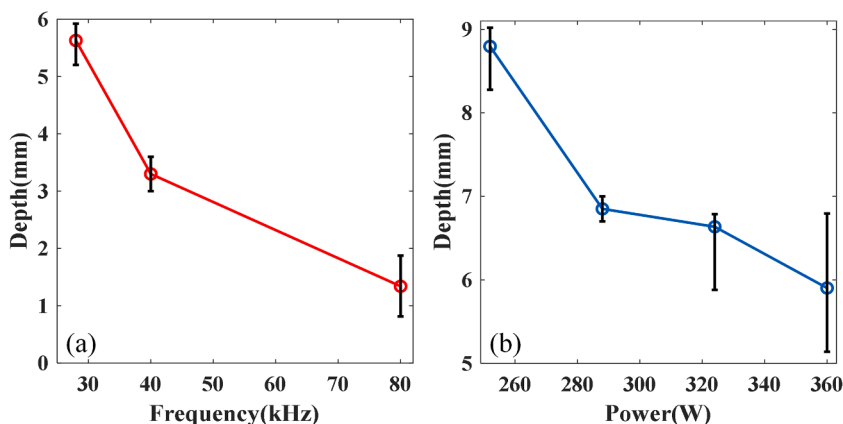


Fig. 7. (a) Effect of acoustic frequency on the depth of the structure below the EPE/water interface at 360 W. (b) Effects of input electric power on the depth of the layer structure below the air/water interface at 28 kHz. The layer structure cannot be observed if the electric power is <252 W. The depths are marked in Fig. 2(e) and Fig. 4(f). The bars and blue (red) circles indicate the vertical floating range of the structure and weighted-average statistical values, respectively. The weight of statistic is defined by ratio of the number of frames with a given depth to the total number of frames.

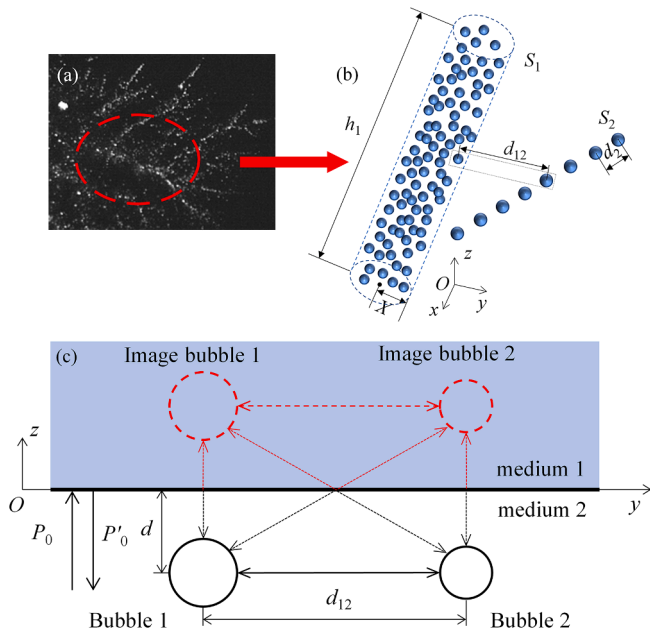


Fig. 8. (a) Top-view picture of the layer structure. (b) Simplified model of the local branch of the layer structure. (c) Schematic illustration of bubble interactions near the interface.

interactions among bubbles along the outer branches of the layer structure were analyzed in our previous study [6]. In this section, we isolated a local branch inside the structure (marked by a dashed circle in Fig. 8(a)), and introduced a model (Fig. 8(b)) to explore the bubble–bubble interactions, and explain how these structures hover stably below a soft interface. The bubbles may follow different paths into an inner branch, as shown in Fig. 3(b), which results in greater bubble concentration in this kind of branch than in outer branches. Therefore, for simplicity, branches S_1 and S_2 were modeled as a column and straight chain of bubbles, respectively. We supposed that all bubbles of uniform radius oscillate in a coupled state in the column, and that the chain-like bubble nuclei (S_2) in the surrounding liquid were attracted to the column (S_1), as shown in Fig. 8(b) [22–24].

We assumed that the equilibrium radius of the bubbles was R_{i0} and that their oscillations were synchronous in S_i ($i = 1, 2$). We chose two representative bubbles from the column and the chain, and simplified them as a bubble pair to analyze the interaction between the column and the chain. The structure hovers at a certain distance from the interface (e.g., the air/water or EPE/water interface). The primary acoustic field and secondary radiation field generated by the bubbles are affected by the properties of the interface, such as diffusion, reflection, and absorption. In general, the mirror-image principle can be used to treat this type of problem [17], whereby the dynamic interactions of the local bubble column and surrounding bubble nuclei are reduced to a four-bubble system, as shown in Fig. 8(c).

If we ignore the effect of bubble coalesce on the length of the column, the dynamic equations for the motion of the column boundary S_1 , and bubble i ($i = 1, 2$) are given by [22–25]

$$\left(X\ddot{X} + \dot{X}^2 \right) \ln \frac{x_c}{X} + \frac{\beta}{2} \dot{X}^2 \left[\left(\frac{X}{x_c} \right)^2 - 1 \right] = -\frac{1}{\rho\beta} (P_{l1} - P_c), \quad (1)$$

$$\alpha_1 \left(1 - \frac{\dot{R}_1}{c} \right) R_1 \ddot{R}_1 + \frac{3}{2} \alpha_2 \left(1 - \frac{\dot{R}_1}{3c} \right) \dot{R}_1^2 = \frac{1}{\rho} \left(1 + \frac{\dot{R}_1}{c} + \frac{R_1}{c} \frac{d}{dt} \right) (P_{B1} - P_c), \quad (2)$$

$$\begin{aligned} & \left(1 - \frac{\dot{R}_2}{c} \right) R_2 \ddot{R}_2 + \frac{3}{2} \left(1 - \frac{\dot{R}_2}{3c} \right) \dot{R}_2^2 \\ &= \frac{1}{\rho} \left(1 + \frac{\dot{R}_2}{c} + \frac{R_2}{c} \frac{d}{dt} \right) (P_{B2} - P_{l2}) - \sum_{k=1}^{N_2-1} \frac{(2R_2 \dot{R}_2^2 + R_2^2 \ddot{R}_2)}{kd_2}, \end{aligned} \quad (3)$$

where R_i ($i = 1, 2$) is the instantaneous radius of bubble i ; X and x_c are the instantaneous and critical radius of S_1 ; ρ and c are the density and sound speed of liquid; β is the volume fraction of gas; $\delta_r = 1/n_1^{1/3}$ is the coupling distance of bubbles inside S_1 with a bubble number density, $n_1; \alpha_1 = (1 + 2\pi R_1 n_1 \delta_r^2)$; $\alpha_2 = (3/2 + 4\pi R_1 n_1 \delta_r^2)$ [20]; and P_c is the liquid pressure. The last term in Eq. (3) is the sum of the secondary radiation pressure from the other bubbles inside S_2 on bubble 2; N_2 is the bubble number; and the coupling coefficient can be defined by $S_{22} = \sum_{k=1}^{N_2-1} \frac{\rho}{kd_2}$ [27], where d_2 is the distance between two adjacent bubbles in S_2 . If we suppose that the liquid inside S_1 is incompressible, one has

$$2N_1 R_1^2 \dot{R}_1 = X \dot{X} h_1, \quad (4)$$

where N_1 is the total number of bubbles in S_1 . The pressure P_{Bj} and P_{lj} are given by

$$P_{Bi} = \left(P_\infty + \frac{2\sigma}{R_{i0}} \right) \left(\frac{R_{i0}}{R_i} \right)^{3\gamma} - \frac{2\sigma}{R_i} - \frac{4\eta \dot{R}_i}{R_i}, \quad (i = 1, 2) \quad (5a)$$

$$P_{li} = P_\infty - P_{si}, \quad (i = 1, 2) \quad (5b)$$

where σ and η are the surface tension coefficient and liquid viscosity, and P_∞ is the ambient pressure at infinity. The pressure perturbation, P_{si} , related to the primary and secondary acoustic wave on the surface of bubble i ($i = 1, 2$) can be expressed as [17]

$$\begin{aligned} P_{si} &= P_a \sin(2\pi f t - k_1 z) + C_R P_a \sin(2\pi f t + k_1 z) \\ &- S_{12} \left(2R_i \dot{R}_j^2 + R_j^2 \ddot{R}_j \right) - S_{CR} \left(2R_i \dot{R}_i^2 + R_i^2 \ddot{R}_i \right), \quad (j = 3 - i) \end{aligned} \quad (6)$$

where the first two terms denote the pressure function of the incident and reflected wave (P_0 and P'_0), the other items represent the secondary radiation. P_a is the acoustic pressure; f is the frequency; d_{12} is the distance between two real bubbles; d is the distance from the two bubbles to the interface; C_R is the acoustic reflection coefficient at the interface; and the coupling coefficients S_{CR} and S_{12} are given by $S_{CR} = \frac{C_R \rho}{2d}$, $S_{12} = S_{21} = \rho \left(\frac{1}{d_{12}} + \frac{C_R}{\sqrt{d_{12}^2 + 4d^2}} \right)$.

The vertical component of the translational motion of bubble i is determined by the acting forces (e.g., the buoyancy force (F_{bi}), primary Bjerknes force (F_{Bpi}), and z -components, F_{Bsi} , of the secondary Bjerknes force, F_{Bsi} ($i = 1, 2$)). These forces are given by [17,27]

$$\begin{aligned} F_{bi} &= \rho g \langle V_i(t) \rangle_T \vec{e}_z, F_{Bpi} = -\langle \nabla_z (P_0(y, t) + P'_0(y, t)) V_i(t) \rangle_T, \\ F_{Bsiy} &= (-1)^{i-1} \left(\frac{\rho}{4\pi d_{12}^2} + \frac{\rho d_{12}}{2\pi (d_{12}^2 + d^2)^{3/2}} \right) \left\langle \dot{V}_i(t) \dot{V}_{(3-i)}(t) \right\rangle_T, \\ F_{Bsiz} &= C_R \left(\frac{\rho d}{2\pi (d_{12}^2 + d^2)^{3/2}} \left\langle \dot{V}_i(t) \dot{V}_{(3-i)}(t) \right\rangle_T + \frac{\rho}{4\pi d^2} \left\langle \dot{V}_i^2(t) \right\rangle_T \right) \vec{e}_z, \quad (i = 1, 2) \end{aligned} \quad (7)$$

where V_i is the volume of bubble i ; g is the gravitational acceleration; F_{Bsiy} (F_{Bsiz}) is the y (z)-component of the secondary Bjerknes force, F_{Bsi} ; $\langle \rangle_T$ denotes a time average over one acoustic period; and \vec{e}_y and \vec{e}_z are the unit vectors in the y and z -directions, respectively.

3.1. Linear approximation

The linear prediction agrees well with the experimental results when the sound field is weak [26]. For a small driving pressure amplitude, $R_i = R_{i0}(1 + r_i)$, ($i = 1, 2$), with $r_i \ll 1$. Combining this with Eqs. (1)–(4), the linear approximation of the equations can be obtained as

$$\begin{cases} \ddot{r}_1 + 2b_1\dot{r}_1 + \omega_{01}^2 r_1 + H_{12}\ddot{r}_2 = P_a e^{-I\omega t} / A_1 \\ \ddot{r}_2 + 2b_2\dot{r}_2 + \omega_{02}^2 r_2 + H_{21}\ddot{r}_1 = P_a e^{-I\omega t} / A_2 \end{cases} \quad (8)$$

where $I = \sqrt{-1}$, b_i is a damping factor, ω_{0i} is the resonant frequency of bubble i , and A_i is the effective mass. This yields

$$\begin{aligned} b_i &= \frac{2\eta}{A_i}, \omega_{0i}^2 = \frac{1}{A_i} \left(3\gamma P_\infty + (3\gamma - 1) \frac{2\sigma}{R_{i0}} \right), H_{i(3-i)} = S_{i(3-i)} \frac{R_{(3-i)0}^3}{A_i}, A_1 \\ &= \rho R_{10}^3 \left(\frac{1}{R_{10}} + 2\delta_r^2 n_1 \pi + \beta \frac{4N_1 (x_c^2 - X_0^2)}{h_1 X_0^2} \right) + S_{CR} R_{10}^3, \\ A_2 &= \rho R_{20}^2 + (S_{22} + S_{CR}) R_{20}^3, \quad (i = 1, 2). \end{aligned} \quad (9)$$

Fig. 9 presents a comparison of the resonant frequency and damping factor for bubble 1, bubble 2, and a single bubble in the unbounded liquid. The calculations were performed with the following parameters: $\eta = 0.001$ kg/(m s), $\sigma = 0.0725$ N/m, $\rho = 998$ kg/m³, $c = 1500$ m/s, $P_\infty = 101$ kPa, and $\gamma = 1.4$. On the basis of the experimental results, we deemed it reasonable to set $x_c = 0.4$ mm, $X_0 = d_{12} = d_2 = 0.2$ mm, h_1

$= 2$ mm, $n_1 = (5 \times 10^{-6}/R_{10})^3 n_0$, and $n_0 = 10^{12}$ m⁻³, $d = 5$ mm, and $N_2 = 10$. In all three cases, the resonant frequency and damping factor decrease with increasing bubble radius. Owing to the coupled effect [28], slightly lower values of the two parameters were obtained for the bubbles in the structures. The coupled strength affects the resonant properties, and the effective mass, A_i , is reduced by a soft boundary, where $S_{CR} R_{10}^3 < 0$. However, according to our estimation, $|S_{CR} R_{10}^3|$ is at least two orders of magnitude lower than the other terms. Notably, the resonant frequencies of the two bubbles are equal at 22.2 μ m, which means that the bubbles of the structure and the chain might be in a state of synchronous resonance.

Assuming that the solution of Eq. (8) has the following form

$$r_i = r_{ia} e^{I\omega t} \quad (10)$$

where r_{ia} is the complex amplitude, $\omega = 2\pi f$, one obtains

$$\begin{cases} -\omega^2 - 2Ib_1\omega + \omega_{01}^2 - H_{12}\omega^2 \\ -H_{21}\omega^2 - \omega^2 - 2Ib_2\omega + \omega_{02}^2 \end{cases} \begin{Bmatrix} r_{1a} \\ r_{2a} \end{Bmatrix} = \begin{Bmatrix} P_a/A_1 \\ P_a/A_2 \end{Bmatrix} \quad (11)$$

with

$$\begin{aligned} r_{ia} &= -\frac{P_a (H_{i(3-i)}\omega^2/A_{3-i} + (\omega_{0(3-i)}^2 - 2Ib_{3-i}\omega - \omega^2)/A_i)}{H_{i(3-i)}H_{(3-i)i}\omega^4 - (\omega_{0i}^2 - 2Ib_i\omega - \omega^2)(\omega_{0(3-i)}^2 - 2Ib_{3-i}\omega - \omega^2)} \\ &= R_{ia} e^{I\theta_i} \end{aligned} \quad (12)$$

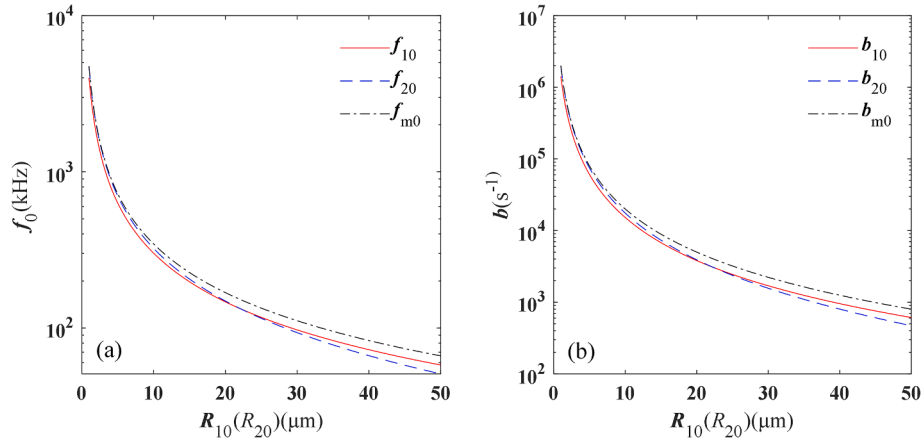


Fig. 9. Comparison of the resonance frequency and damping factor for bubbles close to a soft boundary ($C_R = -1$).

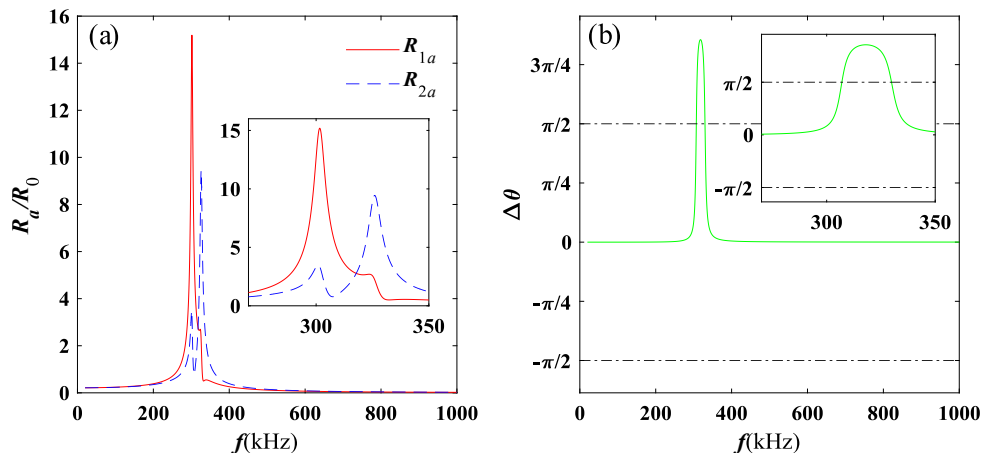


Fig. 10. Frequency response of bubbles near the soft boundary when $R_{10} = R_{20} = 10$ μ m: (a) radial displacement amplitude, (b) phase difference, $\Delta\theta = \pm\frac{\pi}{2}$ are marked by black dotted lines. The subplots show the variation curves in the range of 270–350 kHz.

where R_{ia} is the radial displacement amplitude of the bubble, and θ_i is the initial phase. As detailed in **Appendix B**, the direction of the secondary Bjerknes force between the two bubbles is determined by the phase difference, $\Delta\theta = \theta_1 - \theta_2$. If $-\frac{\pi}{2} < \Delta\theta < \frac{\pi}{2}$, this force is negative and

the two bubbles experience a mutually attractive force; otherwise they experience repulsion.

The relationship between the displacement amplitude (phase difference) and acoustic frequency is presented in **Figs. 10 and 11** by setting

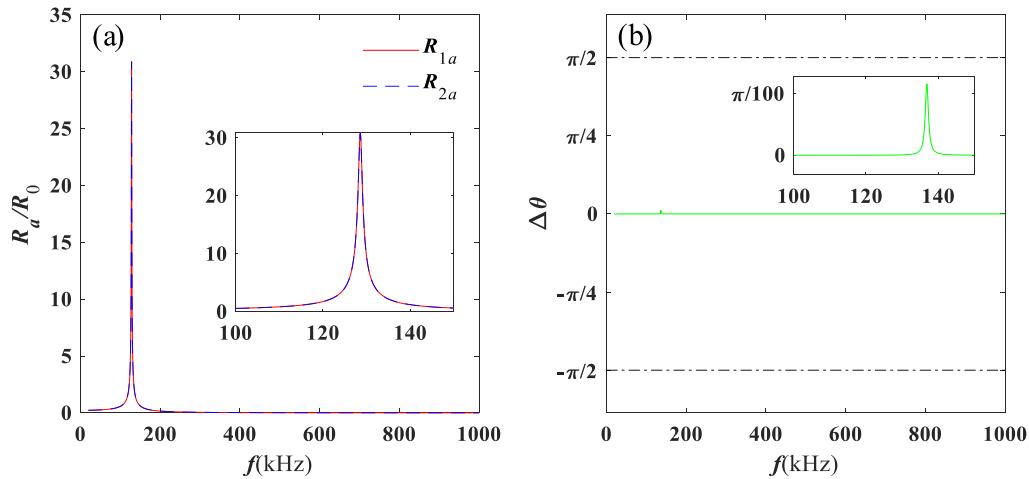


Fig. 11. Frequency response of bubbles near the soft boundary when $R_{10} = R_{20} = 22.2 \mu\text{m}$: (a) radial displacement amplitude, (b) phase difference, $\Delta\theta = \pm\frac{\pi}{2}$ are marked by black dotted lines. The subplots show the variation curves in the range of 100–150 kHz.

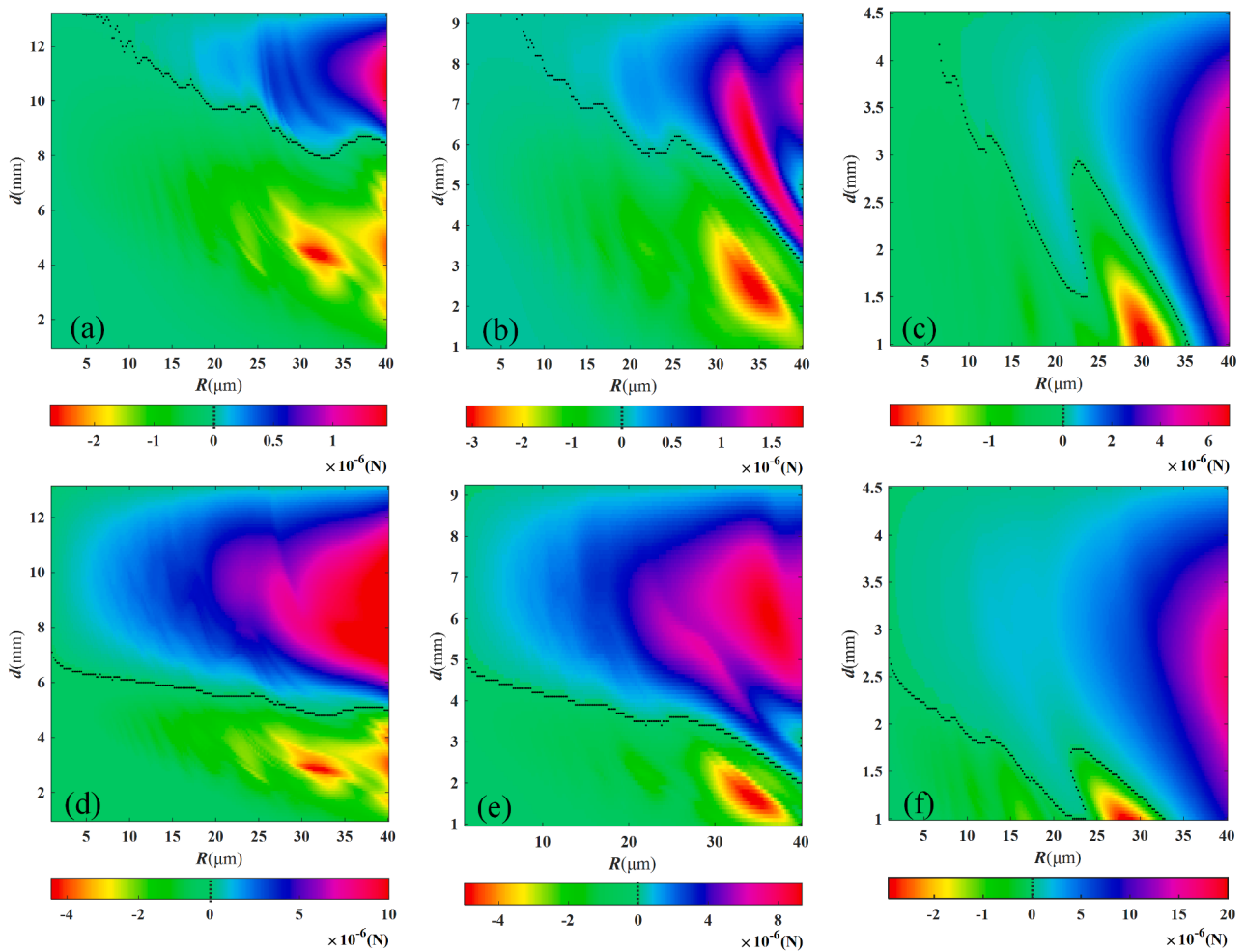


Fig. 12. Effects of bubble radius and distance between layer structure and the interface on the vertical component of the net force of bubble 1 for different acoustic frequencies and pressure amplitudes: (a) 28 kHz, 100 kPa, (b) 40 kHz, 100 kPa, (c) 80 kHz, 100 kPa, (d) 28 kHz, 150 kPa, (e) 40 kHz, 150 kPa, (f) 80 kHz, 150 kPa. Zero net force is marked by the black dotted curve in each map.

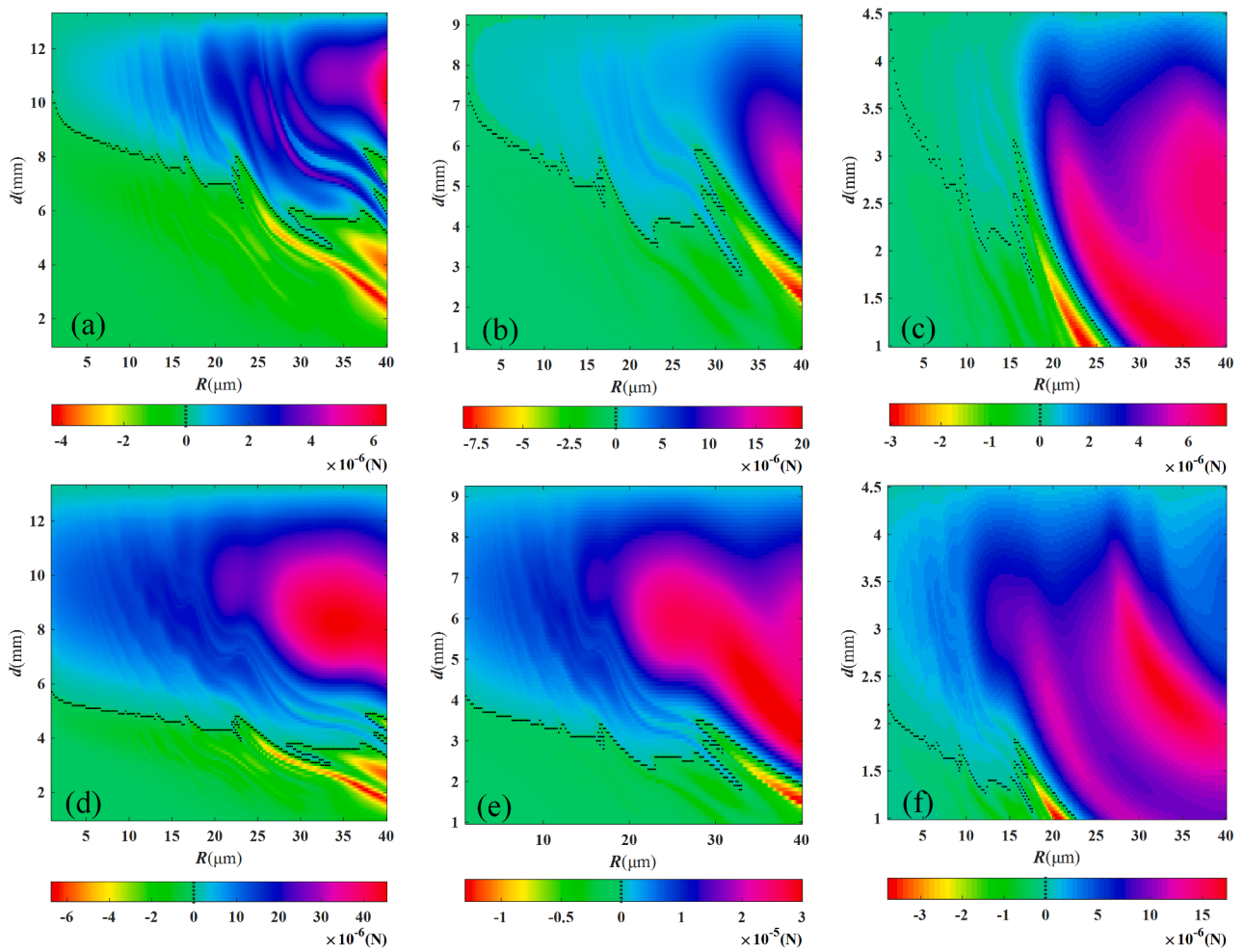


Fig. 13. Effects of bubble radius and distance between layer structure and the interface on the vertical component of the net force of bubble 2 for different acoustic frequencies and pressure amplitudes: (a) 28 kHz, 100 kPa, (b) 40 kHz, 100 kPa, (c) 80 kHz, 100 kPa, (d) 28 kHz, 150 kPa, (e) 40 kHz, 150 kPa, (f) 80 kHz, 150 kPa. Zero net force is marked by the black dotted curve in each map.

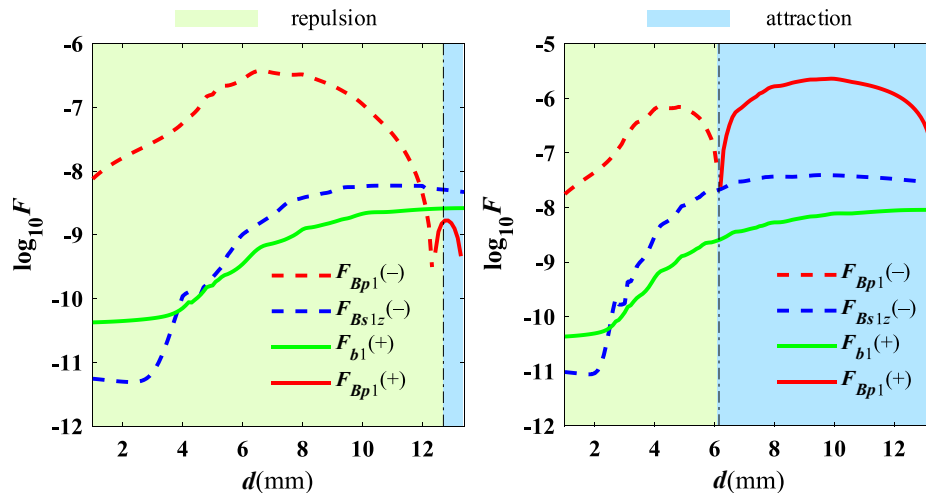


Fig. 14. Forces in the z -direction acting on bubble 1 for $R_{10} = R_{20} = 10 \mu\text{m}$, a frequency of 28 kHz and driving pressures of (a) 100 kPa and (b) 150 kPa. The green background represents a net force < 0 , whereby bubbles are repulsed from the interface, the blue background represents a net force > 0 , whereby bubbles are attracted to the interface.

$R_{10} = R_{20} = 10 \mu\text{m}$ and $R_{10} = R_{20} = 22.2 \mu\text{m}$, respectively. The other parameters used were as follows: $P_a = 10^5 \text{ Pa}$ and $d = 0.11\lambda$ (where λ is the acoustic wavelength in water)[6]. It can be seen that there are

resonant peaks on the frequency–response curves. Although both bubbles have the same radius, the peak frequencies differ; therefore, bubbles in the column and chain have different resonance–response properties.

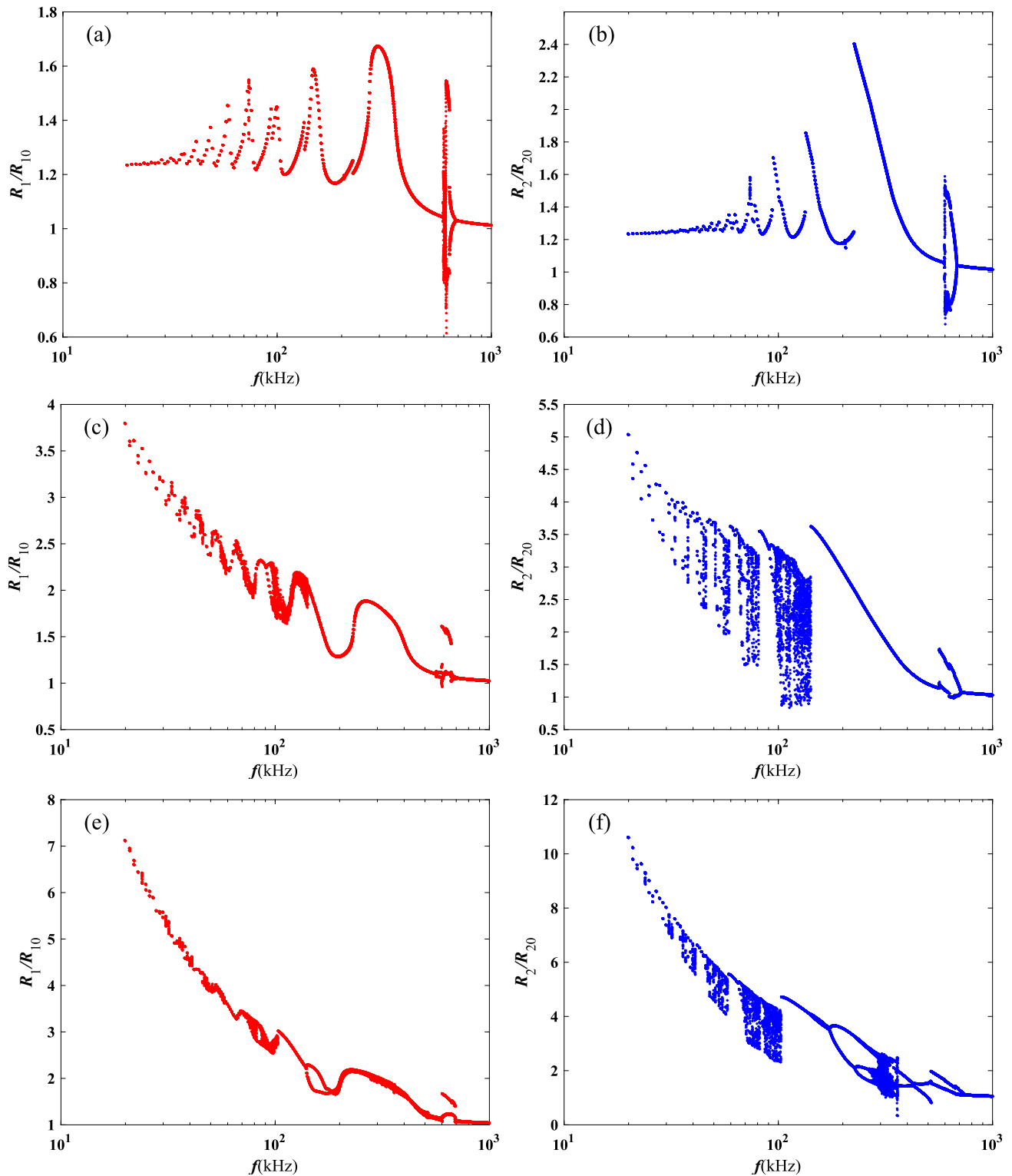


Fig. 15. Bifurcation diagrams of the normalized radius as a function of frequency for $R_{10} = R_{20} = 10 \mu\text{m}$ and different incident sound pressure amplitudes: (a,b) 50 kPa, (c,d) 100 kPa, and (e,f) 150 kPa. Left column: bubble 1, right column: bubble 2. The calculated frequency range is 20–1000 kHz.

For the case of $R_{10} = R_{20} = 10 \mu\text{m}$, the two peak frequencies are about 301.6 and 325.9 kHz (Fig. 10(a)), while the critical frequencies with the phase difference is equal to $\frac{\pi}{2}$ is about 307.1 kHz and 329.9 kHz, respectively (Fig. 10(b)). When the acoustic frequency is between the critical frequencies, the two bubbles repel each other, which might result in a destruction of the layer structure. For the case of

$R_{10} = R_{20} = 22.2 \mu\text{m}$, the peak frequencies are almost the same (Fig. 9 (a)), and the phase difference is much less than $\frac{\pi}{2}$ over the entire calculated frequency range (Fig. 11(b)); therefore, the bubbles attract each other. Therefore, bubble columns are more likely to attract bubbles of similar size in a low-frequency cavitation field.

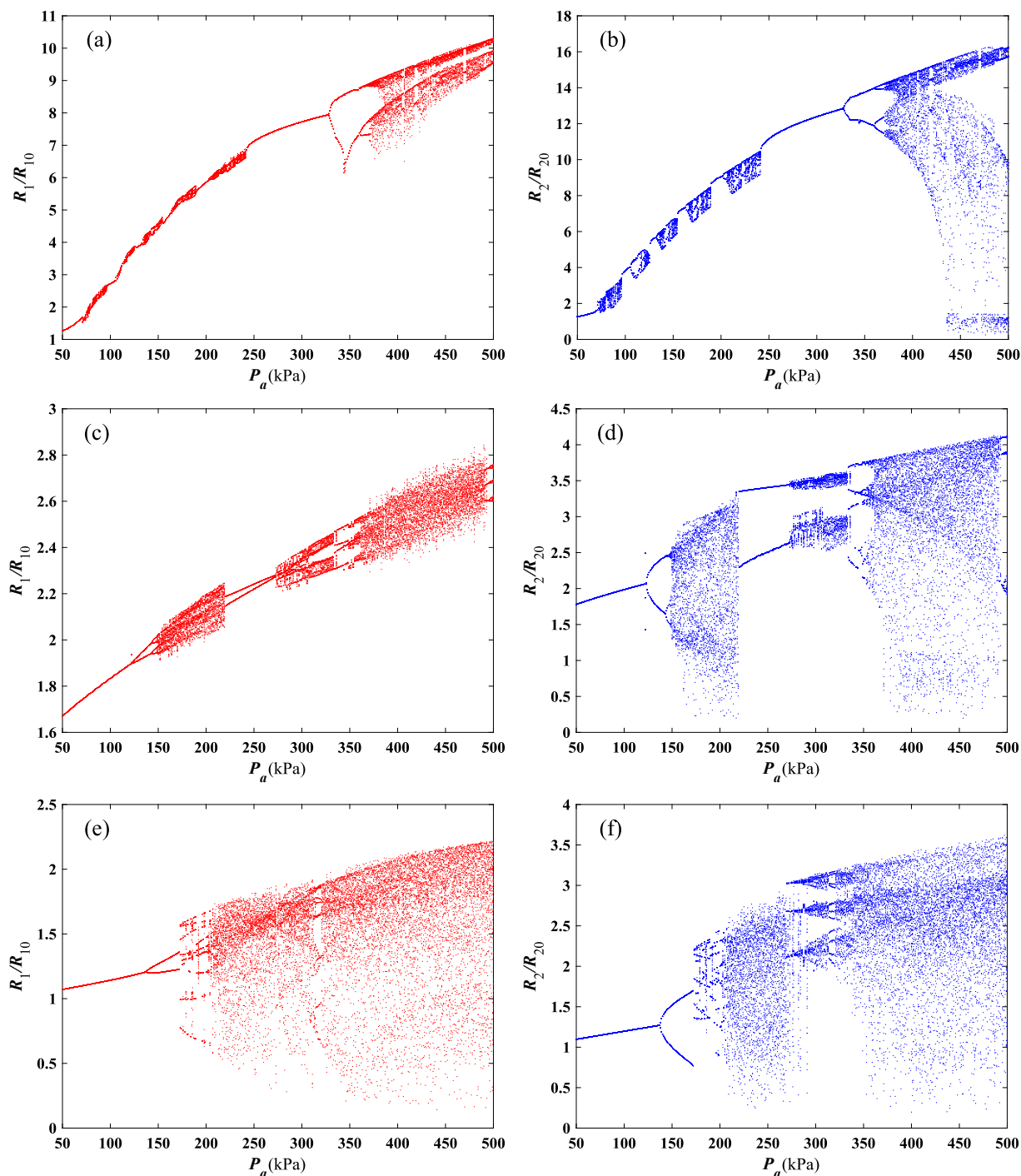


Fig. 16. Bifurcation diagrams of the normalized radius as a function of incident sound pressure amplitude for $R_{10} = R_{20} = 10 \mu\text{m}$ and different frequencies: (a,b) 40 kHz, (c,d) 300 kHz, and (e,f) 500 kHz. Left column: bubble 1; right column: bubble 2. The calculated pressure range is 50–500 kPa.

3.2. Numerical analysis

The bubble structures were observed to translate in a defined layer in the water (Fig. 7) below the air/water and EPE/water interfaces, which indicates that the forces acting on the bubbles within the clusters were balanced in the vertical direction. Buoyancy and Bjerknes forces play important roles in the motions of bubbles. Maps of the vertical net force on bubbles 1 and 2 are shown in Figs. 12 and 13, where the influence of distance to the interface and bubble radius are considered by setting $R_{10} = R_{20}$. The maximum net force is located in the region where the bubble radius is $> 20 \mu\text{m}$, and a repulsive net force is obtained when the distance is

shorter than that marked by the dotted curve. Therefore, there is a repulsive region below the interface, which might be crucial for the formation of the hovering bubble structure. Figs. 12 and 13 show that the repulsive area shrinks with increasing acoustic frequency because the maximum radii and distance of the repulsive region decrease. If we increase the pressure amplitude, the critical distance at which the forces are balanced may be reduced. The results are in good agreement with the experimental measurements (Fig. 7). The dotted curve is far less smooth for the bubble inside the chain (bubble 2) and contains many peaks. Moreover, some bubbles hovered at different distances, similar to the cases exhibited in Fig. 2(f) and Fig. 4(f), where a hat-like structure was observed.

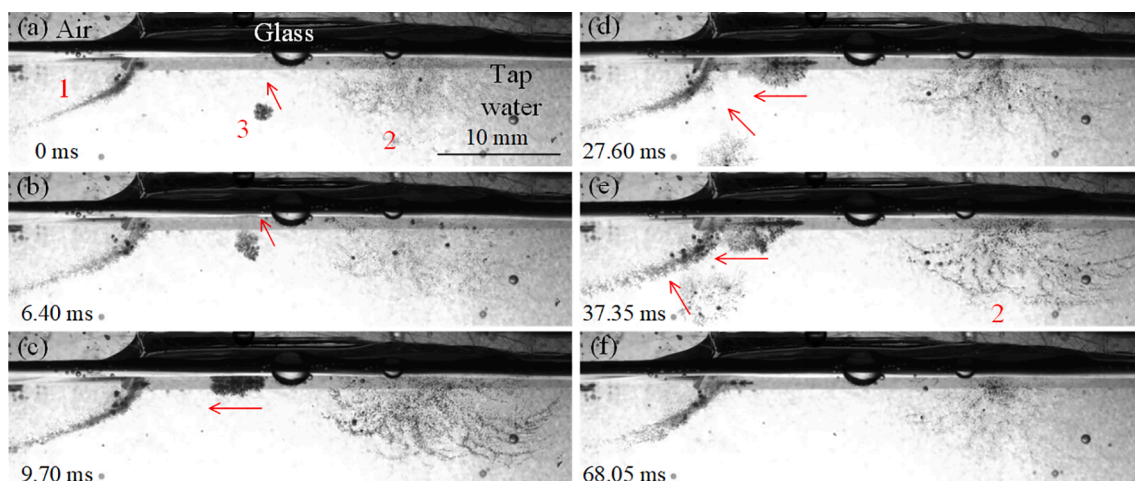


Fig. A1. Evolution of bubble clusters below the glass (Supplementary video 7, side view). The frequency was 28 kHz and electric power was 360 W. The red arrows represent the direction of motion of the bubble clusters. Evolution of bubble cluster was similar below the bottom of beaker (Supplementary video 8, side view, the video height approx. 18.3 mm). There is no water inside the beaker.

To analyze the contribution of the forces on the hovering status of the structure, we simulated the effects of the distance on buoyancy, and on the primary and secondary Bjerknes forces, as shown in Fig. 14. In general, the primary Bjerknes force is greater than the other two forces. However, the buoyancy and secondary Bjerknes forces increase with distance, whereas the primary force decreases after the distance exceeds a certain value (about 8 mm at 28 kHz and 100 kPa, Fig. 14(a)); hence, a critical state (marked by the vertical dashed line) can be achieved. Therefore, the hovering phenomenon is related to the enhancement of the secondary radiation. When the pressure increases to 150 kPa at 28 kHz, the critical distance shifts to the left owing to the reversal of the primary Bjerknes force, as shown in Fig. 14(b). Therefore, the primary force distinctly affects the hovering position of the structure.

The hovering depth of the structure and the bubble motions are strongly affected by the acoustic frequency and pressure, and the shape evolution of the structure may depend on the coupled strength of bubbles. In addition, the coupling behavior can enhance the dynamic nonlinearity of the bubbles [29]. Fig. 15 presents the bifurcation diagrams of dimensionless bubble radius as a function of frequency at difference acoustic pressures (50, 100, and 150 kPa). Because of the coupled effect, the oscillations of the bubbles are suppressed [30], and the suppression on bubble 1 in the column is stronger. From Fig. 15(a, b), the resonant frequencies of bubbles 1 and 2 are estimated as 295 and 227 kHz, respectively, which are lower than the linear values (Fig. 10). For an acoustic pressure of 50 kPa, many harmonic resonant peaks on the curves can be observed, especially at frequencies below 100 kHz. At pressures above 100 kPa, bubble oscillations are enhanced, resulting in a chaotic response, especially for bubbles outside the column. Nevertheless, bubbles in the column have a strong synergistic influence on the surrounding bubbles or gas nuclei; therefore, bubbles outside the column are attracted and merge.

The chaotic oscillations of bubbles can be excited by high-intensity ultrasound, and it is difficult to accurately predict and control bubble behavior [31–33]. Fig. 16 shows the bubble bifurcation plots for frequencies of 40, 300, and 500 kHz. The chaotic patterns of the two bubbles are different, and the behavior of bubble 2 is more complex. Because of the strong interaction between the bubbles, their plots have similar bifurcation points and chaotic pressure ranges. At 40 kHz, the bubble alternates between simple periodic and chaotic states when the pressure is below 200 kPa, and simple periodic motion is observed in the range of 242–327 kPa (Fig. 16(a)). However, at 300 kHz (500 kHz), this motion only occurs at pressures lower than ~123 kPa (~137 kPa) (Fig. 16(c, e)). Therefore, when bubbles are driven by low-frequency ultrasound, large amplitude nonlinear pulsations are easily excited,

which may lead to a strong collapse. Under these conditions, inertial cavitation should be the primary mode of cavitation. If the driving frequency is higher 100 kHz, the primary mode is more likely to be stable bubble pulsation [34], although high driving pressures may decrease the stability and results in a chaotic bubble response. Therefore, we predict that hat-like layer structures of bubbles exist in intense cavitation fields where bubbles oscillate violently. At 80 kHz, cavitation is relatively weak, and nonlinear stability might play a role in the formation of the layer structure. Because the oscillation amplitude of bubbles is relatively small, the synergistic influence of the bubble clusters is weak, making it more difficult to form a large hat-like structure.

4. Conclusion and discussion

We investigated the bubble structures just beneath the air/water and EPE/water interface experimentally. The formation and evolution of the layer structure were similar for the two interfaces. The layer structures were generated by the upward floating of spherical clusters, which grew from a source bubble and attracted other bubbles. The source bubbles had three possible origins: attached bubble nuclei at the interface, floating bubbles in the bulk liquid, and bubbles at the surface of the ultrasonic transducer. The structure of the accumulated layer of bubbles was affected by the boundary shape, and acquired a similar profile to the interface. The frequency also affected the morphology of the structures, with a hat-like structure observed at 28 and 40 kHz, and a layer structure consisting of discrete bubble clusters observed at 80 kHz. The top-view images showed that bubbles accumulated in a typical branch structure.

A branching model was developed to simulate the bubble interactions. We found that the primary sound field plays an important role in the generation of the structure. A higher acoustic frequency and pressure could lead to a decrease in the distance between the structure and the interface. A hat-like layer structure of bubbles is more likely to exist in an intense cavitation field where bubbles oscillate violently, whereas a layer structures with discrete spherical clusters is more likely to exist in a relatively weak cavitation field, where stable and inertial cavitation coexist. The theoretical predictions agreed well with the experimental observations; therefore, this simplified model could be used to simulate the interaction between bubbles in the layer structure and surrounding bubble nuclei. Our theoretical analysis reveals that the cavitation intensity is closely related to the aggregation morphology of bubbles.

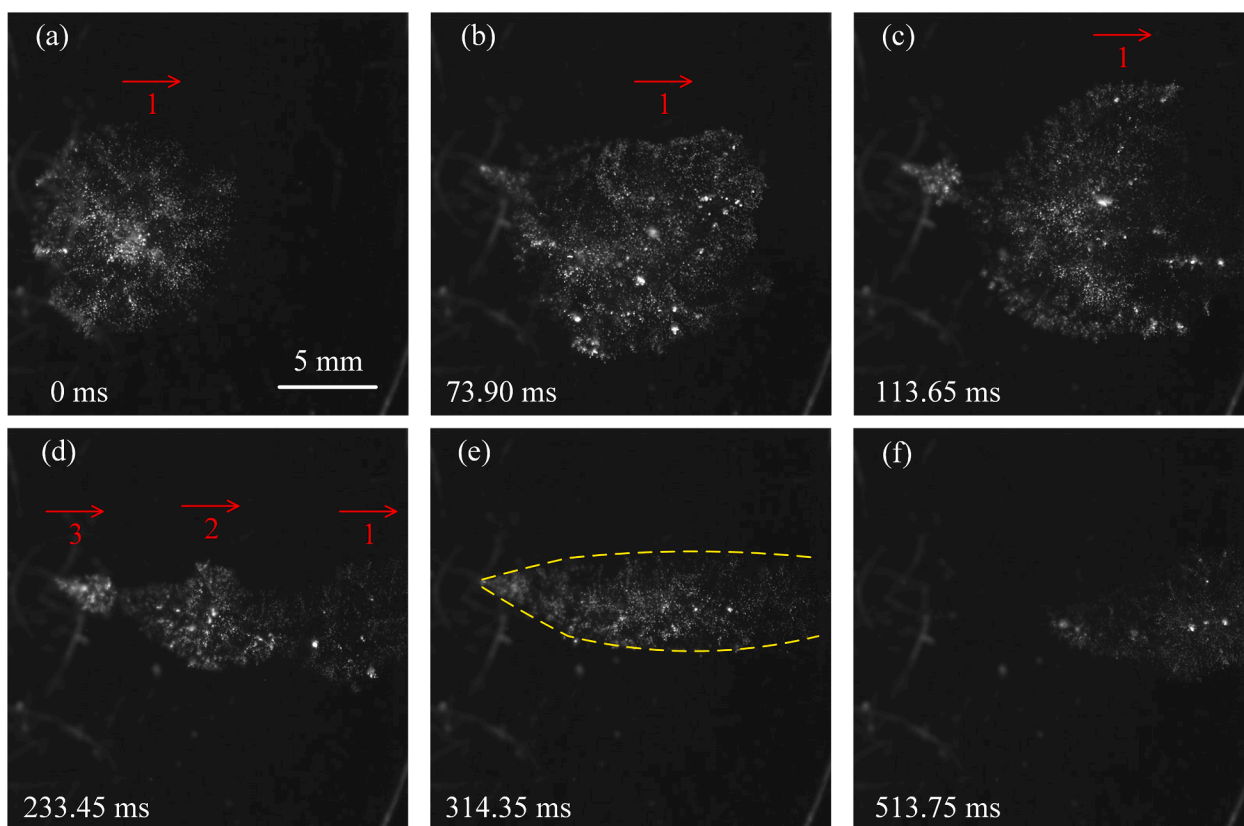


Fig. A2. Evolution of bubble clusters below the bottom of a beaker (Supplementary video 9, top view). The frequency was 28 kHz and electric power was 360 W. There is no water inside the beaker. The bubble clusters are marked by '1', '2' and '3'. The red arrows represent the direction of motion of the clusters. The yellow dashed line represents the boundary of the bubble streamer.

CRediT authorship contribution statement

Fan Li: Investigation, Conceptualization, Formal analysis, Software, Validation, Writing – original draft. **Chenyang Huang:** Formal analysis, Software, Validation. **Xianmei Zhang:** Supervision, Formal analysis, Methodology. **Chenghui Wang:** Investigation, Conceptualization, Formal analysis, Methodology, Supervision, Writing – review & editing. **Jing Hu:** Formal analysis, Writing – review & editing. **Shi Chen:** Methodology, Writing – review & editing. **Hua Tian:** Supervision, Formal analysis. **Zhuangzhi Shen:** Methodology, Supervision, Writing – review & editing. **Jianzhong Guo:** Methodology, Writing – review & editing. **Shuyu Lin:** Formal analysis, Supervision.

Declaration of Competing Interest

The authors declare that they have no known competing financial

interests or personal relationships that could have appeared to influence the work reported in this paper.

Data availability

Data will be made available on request.

Acknowledgements

This work was supported by the National Natural Science Foundation of China (Grant Nos.11974232, 11727813) and Yulin Science and Technology Bureau (CX-2022-178).

Appendix A.: Behaviors of bubbles below glass/water interface

The bubble clusters below flat glass ($40 \times 40 \times 5 \text{ mm}^3$, density of $2.5 \times 10^3 \text{ kg/m}^3$) were captured by a high-speed camera at 20,000 fps; the experimental setup was described in Ref. [6]. The acoustic velocity in the glass is about 4,000 m/s, and the acoustic reflection coefficient at the glass/water interface is about 0.74. Fig. A1 shows that a spherical bubble cluster (cluster 3 in Fig. A1(a)) floated to the water/glass interface, which was different from the hovering phenomenon observed under the soft boundary. Then, the cluster evolved into a hemispherical cluster, and finally merged along the water/glass interface into cluster 1 under the free water surface on the left side of each image. To facilitate observation, we used a beaker instead of the flat glass to observe the evolution of the bubble clusters, as shown in Fig. A2. The upward floating spherical bubble clusters did not collapse completely when they collided with the bottom of the beaker, but formed a hemispherical cluster that moved along the bottom surface. Increasingly more clusters formed in a row (Fig. A2(d)), leading to the formation of a streamer, as shown in Fig. A2(e).

Appendix B

The instantaneous radius of bubble i predicted by linear theory (Eq. (10)) can be expressed as

$$R_i = R_{i0} + \operatorname{Re}(R_{i0} R_{ia} e^{j(\omega t + \theta_i)}) = R_{i0} + R_{i0} R_{ia} \cos(\omega t + \theta_i), \quad (\text{B1})$$

where Re denotes the real part of the formula. The y -component of the secondary Bjerknes force on bubble 1 (Eq. (7)) can be transformed as follows:

$$F_{B_{s1y}} = 16\pi^2 R_1^2 R_2^2 \left(\frac{\rho}{4\pi d_{12}^2} + \frac{\rho d_{12}}{2\pi(d_{12}^2 + d^2)^{3/2}} \right) \langle \dot{R}_1 \dot{R}_2 \rangle_T. \quad (\text{B2})$$

The sign of $F_{B_{s1y}}$ is determined by $\langle \dot{R}_1 \dot{R}_2 \rangle_T$. If $\langle \dot{R}_1 \dot{R}_2 \rangle_T > 0$, $F_{B_{s1y}} > 0$ and the two bubbles attract each other. Substituting Eq. (A1) into $\langle \dot{R}_1 \dot{R}_2 \rangle_T$ yields

$$\langle \dot{R}_1 \dot{R}_2 \rangle_T = R_{10} R_{1a} R_{20} R_{2a} \int_0^T \sin(\omega t + \theta_1) \sin(\omega t + \theta_2) dt = R_{10} R_{1a} R_{20} R_{2a} \cos \Delta \theta \int_{\theta_2/\omega}^{T-\theta_1/\omega} \sin^2(\omega t) dt \quad (\text{B3})$$

where all terms are positive except for $\cos \Delta \theta$. If $-\frac{\pi}{2} < \Delta \theta < \frac{\pi}{2}$, $\cos \Delta \theta > 0$, and the force is attractive; whereas $-\pi < \Delta \theta < -\frac{\pi}{2}$ or $\frac{\pi}{2} < \Delta \theta < \pi$, $\cos \Delta \theta < 0$, and the force is repulsive.

Appendix C. Supplementary data

Supplementary data to this article can be found online at <https://doi.org/10.1016/j.ultsonch.2023.106500>.

References

- [1] K.S. Suslick, *Sonochemistry*, Science 247 (4949) (1990) 1439–1445.
- [2] G.L. Chahine, A. Kapahi, J.K. Choi, C.T. Hsiao, Modeling of surface cleaning by cavitation bubble dynamics and collapse, *Ultrason. Sonochem.* 29 (2016) 528–549, <https://doi.org/10.1016/j.ultsonch.2015.04.026>.
- [3] S. Kooij, A. Astefanei, G.L. Cortals, D. Bonn, Size distributions of droplets produced by ultrasonic nebulizers, *Sci. Rep.* 9 (2019) 1–8, <https://doi.org/10.1038/s41598-019-42599-8>.
- [4] J. González-García, V. Sáez, I. Tudela, M.I. Díez-García, M.D. Esclapez, O. Louisnard, Sonochemical treatment of water polluted by chlorinated organocompounds, A review, *Water (Switzerland)* 2 (2010) 28–74, <https://doi.org/10.3390/w2010028>.
- [5] R. Mettin, *Bubble structures in acoustic cavitation*, Mod. Trends Appl. Res. Signpost. (2005) 1–36.
- [6] F. Li, C. Huang, X. Zhang, C. Wang, J. Guo, S. Lin, Z. Shen, H. Tian, Structure of bubble cluster adjacent to the water surface in the ultrasonic field, *Ultrasonics* 132 (2023), 106992, <https://doi.org/10.1016/j.ultras.2023.106992>.
- [7] I. Akhatov, U. Parlitz, W. Lauterborn, Pattern formation in acoustic cavitation, *J. Acoust. Soc. Am.* 96 (1994) 3627–3635, <https://doi.org/10.1121/1.410580>.
- [8] I. Akhatov, U. Parlitz, W. Lauterborn, Towards a theory of self-organization phenomena in bubble-liquid mixtures, *Phys. Rev. E - Stat. Physics, Plasmas, Fluids, Relat. Interdiscip. Top.* 54 (1996) 4990–5003, <https://doi.org/10.1103/physreve.54.4990>.
- [9] J. Appel, P. Koch, R. Mettin, D. Krefting, W. Lauterborn, Stereoscopic high-speed recording of bubble filaments, *Ultrason. Sonochem.* 11 (2004) 39–42, [https://doi.org/10.1016/S1350-4177\(03\)00111-1](https://doi.org/10.1016/S1350-4177(03)00111-1).
- [10] R. Mettin, S. Luther, C.D. Ohl, W. Lauterborn, Acoustic cavitation structures and simulations by a particle model, *Ultrason. Sonochem.* 6 (1999) 25–29, [https://doi.org/10.1016/S1350-4177\(98\)00025-X](https://doi.org/10.1016/S1350-4177(98)00025-X).
- [11] J.R. Blake, U. Parlitz, R. Mettin, S. Luther, I. Akhatov, M. Voss, W. Lauterborn, Spatio-temporal dynamics of acoustic cavitation bubble clouds, *Philos. Trans. R. Soc. A Math. Phys. Eng. Sci.* 357 (1751) (1999) 313–334.
- [12] R. Mettin, C.-D. Ohl, W. Lauterborn, Particle Approach to Structure Formation in Acoustic Cavitation, in: L.A. Crum, T.J. Mason, J.L. Reisse, K.S. Suslick (Eds.), *Sonochemistry and Sonoluminescence*, Springer Netherlands, Dordrecht, 1999, pp. 139–144.
- [13] R. Mettin, P. Koch, W. Lauterborn, D. Krefting, Modeling Acoustic Cavitation with Bubble Redistribution, *Sixth Int. Symp. Cavitation*. (2006) 1–5.
- [14] F. Li, X. Zhang, H. Tian, J. Hu, S. Chen, R. Mo, C. Wang, J. Guo, Interactions of bubbles in acoustic Lichtenberg figure, *Ultrason. Sonochem.* 87 (2022), 106057, <https://doi.org/10.1016/j.ultsonch.2022.106057>.
- [15] S. Kou, W. Chen, Y. Wu, G. Zhao, Translation of cavitation bubble near the different walls, *Ultrason. Sonochem.* 94 (2023), 106352, <https://doi.org/10.1016/j.ultsonch.2023.106352>.
- [16] R. Manasseh, A. Ooi, Frequencies of acoustically interacting bubbles, *Bubble Sci. Eng. Technol.* 1 (2009) 58–74, <https://doi.org/10.1179/175889709X446552>.
- [17] E. van 't Wout, C. Feuillade, Proximity resonances of water-entrained air bubbles near acoustically reflecting boundaries, *J. Acoust. Soc. Am.* 149 (4) (2021) 2477–2491.
- [18] R. Mettin, I. Akhatov, U. Parlitz, C.D. Ohl, W. Lauterborn, Bjerknes forces between small cavitation bubbles in a strong acoustic field, *Phys. Rev. E - Stat. Physics, Plasmas, Fluids, Relat. Interdiscip. Top.* 56 (1997) 2924–2931, <https://doi.org/10.1103/PhysRevE.56.2924>.
- [19] A.G. Athanassiadis, Z. Ma, N. Moreno-Gomez, K. Melde, E. Choi, R. Goyal, P. Fischer, Ultrasound-Responsive Systems as Components for Smart Materials, *Chem. Rev.* 122 (2022) 5165–5208, <https://doi.org/10.1021/acs.chemrev.1c00622>.
- [20] A.A. Atchley, A. Prosperetti, The crevice model of bubble nucleation, *J. Acoust. Soc. Am.* 86 (1989) 1065–1084, <https://doi.org/10.1121/1.398098>.
- [21] C. Wu, N. Nakagawa, Y. Sekiguchi, Observation of multibubble phenomena in an ultrasonic reactor, *Exp. Therm. Fluid Sci.* 31 (2007) 1083–1089, <https://doi.org/10.1016/j.expthermflusci.2006.11.005>.
- [22] W. Zhang, Y. An, Instability of a bubble chain, *Phys. Rev. E - Stat. Nonlinear, Soft Matter Phys.* 87 (2013) 5–10, <https://doi.org/10.1103/PhysRevE.87.053023>.
- [23] Y. An, Formulation of multibubble cavitation, *Phys. Rev. E - Stat. Nonlinear, Soft Matter Phys.* 83 (2011) 2–7, <https://doi.org/10.1103/PhysRevE.83.066313>.
- [24] E.S. Nasibullaeva, I.S. Akhatov, Bubble cluster dynamics in an acoustic field, *J. Acoust. Soc. Am.* 133 (2013) 3727–3738, <https://doi.org/10.1121/1.4802906>.
- [25] I. Hansson, K.A. Mørch, The dynamics of cavity clusters in ultrasonic (vibratory) cavitation erosion, *J. Appl. Phys.* 51 (1980) 4651–4658. Doi: 10.1063/1.328335.
- [26] M. Arora, C.D. Ohl, D. Lohse, M. Arora, C.D. Ohl, D. Lohse, Effect of nuclei concentration on cavitation cluster dynamics, 3432 (2013). Doi: 10.1121/1.2722045.
- [27] K. Yasui, Y. Iida, T. Tuziuti, T. Kozuka, A. Towata, Strongly interacting bubbles under an ultrasonic horn, (2008) 1–10. Doi: 10.1103/PhysRevE.77.016609.
- [28] E.M.B. Payne, S.J. Illesinghe, A. Ooi, R. Manasseh, Symmetric mode resonance of bubbles attached to a rigid boundary, *J. Acoust. Soc. Am.* 118 (2005) 2841–2849, <https://doi.org/10.1121/1.2062268>.
- [29] B.Q.H. Nguyen, I.S. Maksymov, S.A. Suslov, Spectrally wide acoustic frequency combs generated using oscillations of polydisperse gas bubble clusters in liquids, *Phys. Rev. E* 104 (2021), <https://doi.org/10.1103/PhysRevE.104.035104>.
- [30] C.-H. Wang, J.-C. Cheng, Interaction of a bubble and a bubble cluster in an ultrasonic field, *Chinese Phys. B* 22 (1) (2013) 014304.
- [31] S. Behnia, A. Jafari, W. Soltanpoor, O. Jahanbakhsh, Nonlinear transitions of a spherical cavitation bubble, *Chaos, Solitons Fractals* 41 (2009) 818–828, <https://doi.org/10.1016/j.chaos.2008.04.011>.
- [32] S. Behnia, A.J. Sojehrood, W. Soltanpoor, O. Jahanbakhsh, Suppressing chaotic oscillations of a spherical cavitation bubble through applying a periodic perturbation, *Ultrason. Sonochem.* 16 (2009) 502–511, <https://doi.org/10.1016/j.ultsonch.2008.12.016>.
- [33] U. Parlitz, V. Englisch, C. Scheffczyk, W. Lauterborn, Bifurcation structure of bubble oscillators, *J. Acoust. Soc. Am.* 88 (1990) 1061–1077, <https://doi.org/10.1121/1.399855>.
- [34] J. Lee, S. Yang, Antisolvent sonocrystallisation of sodium chloride and the evaluation of the ultrasound energy using modified classical nucleation theory, *Crystals* 8 (2018) 17–22, <https://doi.org/10.3390/cryst8080320>.